

# Electron Heat Flux and Whistler Instability in the Earth's Magnetosheath

Ida Svenningsson,<sup>1,2,3</sup> Emiliya Yordanova,<sup>1</sup> Yuri V. Khotyaintsev,<sup>1,2</sup> Mats Andr,<sup>1</sup> Giulia Cozzani,<sup>4</sup> Alexandros Chasapis,<sup>5</sup> and Steven J. Schwartz<sup>5,6</sup>

<sup>1</sup>Swedish Institute of Space Physics, Uppsala 751 21, Sweden

<sup>2</sup>Department of Physics and Astronomy, Uppsala University, Uppsala 751 20, Sweden

<sup>3</sup>Department of Physics, Chalmers University of Technology, Gteborg 412 96, Sweden

<sup>4</sup>Laboratory of Physics and Chemistry of the Environment and Space (LPC2E), OSUC, Univ Orleans, CNRS, CNES, 45071 Orleans, France

<sup>5</sup>Laboratory for Atmospheric and Space Physics, University of Colorado, Boulder, Colorado 80303, USA

<sup>6</sup>Department of Physics, Imperial College London, London, SW7 2AZ, UK

(Dated: November 14, 2025)

Despite heat flux's role in regulating energy conversion in collisionless plasmas, its properties and evolution in the magnetosheath downstream of the Earth's bow shock are scarcely explored. We use MMS *in situ* measurements to quantify and characterize the electron heat flux in the magnetosheath. We find that the heat flux is shaped by the magnetosheath magnetic field as it drapes around the magnetosphere. While it is affected by solar wind upstream conditions and increases with magnetic field strength, it is not substantially changed by local magnetosheath processes. Also, the heat flux is limited by whistler instability thresholds.

*Introduction* - Electrons control the thermal energy transfer in plasmas due to their low mass compared to ions [1], making the electron heat flux central to the total energy budget. The collisional Spitzer-Hrm [2] heat conduction description breaks down in collisionless plasmas [3], and instead, wave-particle interactions are believed to suppress the heat flux on ion and electron kinetic scales in the heliospheric [4] and astrophysical plasmas [1, 5].

The electron heat flux  $\mathbf{q}_e$  is defined as the third-order moment of the electron velocity distribution function (eVDF):

$$\mathbf{q}_e = \frac{m_e}{2} \int f_e(\mathbf{v}) |\mathbf{w}|^2 \mathbf{w} d^3v, \quad (1)$$

where  $f_e(\mathbf{v})$  is the eVDF,  $\mathbf{w} = \mathbf{v} - \mathbf{V}_e$  is the velocity  $\mathbf{v}$  in the electron bulk flow ( $\mathbf{V}_e$ ) frame, and  $m_e$  the electron mass. The heat flux can be calculated directly from the eVDF in spacecraft observations [3, 4, 6–8]. However, since  $\mathbf{q}_e$  is sensitive to noise related to low count rates, detailed calculations of  $\mathbf{q}_e$  from spacecraft data have mostly been done for case studies [7, 8]. In the solar wind (SW),  $\mathbf{q}_e$  can be obtained by fitting the eVDF core, halo, and strahl components as drifting bi-Maxwellians [9, 10]. In hybrid simulations,  $\mathbf{q}_e$  can be inferred through thermodynamic closures such as Landau-fluid (LF) type closures [11, 12]. Data-driven closures using machine learning [13] and sparse regression [14] have also been suggested. However, it remains a challenge to estimate  $\mathbf{q}_e$  in spacecraft data, notably when the eVDF is strongly non-Maxwellian [15].

Collisionless shocks are associated with strong particle acceleration and heating in various astrophysical environments such as supernova remnants [16], interplanetary shocks [17, 18], and planetary bow shocks [19, 20]. Among these, the Earth's bow shock (BS) is uniquely accessible to *in situ* measurements of electron dynam-

ics. At the BS, electrons are accelerated and heated adiabatically, creating separated hot and cold components. Additionally, non-adiabatic effects due to, e.g., wave-particle interactions [21] become significant at high Mach numbers in the the de Hoffmann-Teller (HT) reference frame [22]. This heating is expected to change  $\mathbf{q}_e$ , but the resulting evolution of  $\mathbf{q}_e$  across the BS is not known. Moreover,  $\mathbf{q}_e$  may be altered by reconnecting current sheets [23–28] or wave-particle interactions [29–33] in the downstream magnetosheath (MSH) region, or magnetic reconnection at the magnetopause (MP) [8, 34]. The relevant space mission allowing the access to electron scales is the Magnetospheric Multiscale (MMS) mission [35], equipped with state-of-the-art instrumentation, permitting the estimation of higher-order moments of the eVDF, such as the heat flux.

In the SW,  $\mathbf{q}_e$  can be regulated by different wave instabilities, of which the whistler wave dominates for  $\beta_{e\parallel} \gtrsim 0.1$  [9], where  $\beta_{e\parallel} = 2\mu_0 n_e T_{e\parallel} / B^2$  and  $n_e$  and  $T_{e\parallel}$  are the electron density and temperature parallel to the magnetic field  $\mathbf{B}$ , and  $B = |\mathbf{B}|$ . Heat flux instabilities can generate both parallel-propagating [9] and highly oblique [36] whistler waves, the interplay of which results in a heat flux reduction [37].

Whistler waves are regularly observed in the MSH. While the most commonly proposed generation mechanism requires a high electron temperature anisotropy [38], whistler waves are not typically associated with the high electron temperature anisotropy required to trigger waves [30]. This can be partly explained by highly non-Maxwellian eVDFs [29, 39]. Therefore, heat flux instabilities should be investigated as alternative candidates for whistler wave generation.

To explore the poorly understood nature of electron heat flux downstream of collisionless shocks, we use measurements from the MMS mission to statistically study

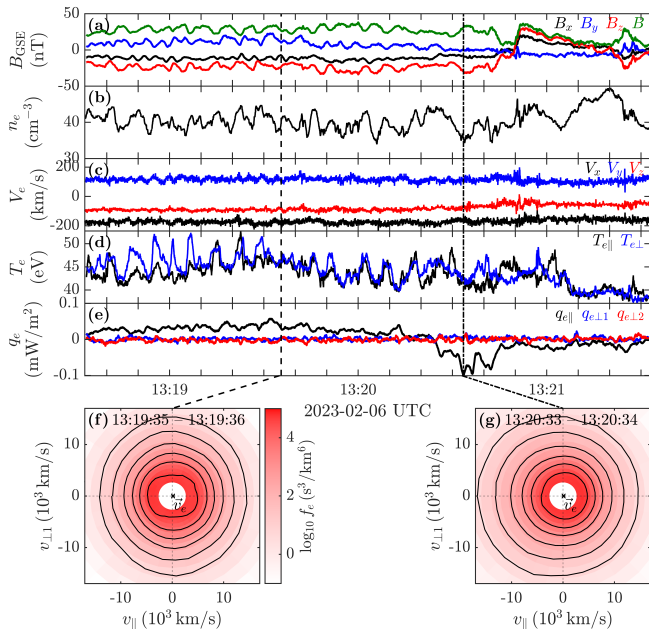


Figure 1. Three-minute interval from the MSH. MMS measurements of the magnetic field  $\mathbf{B}$  (a) and the electron moments: (b) density  $n_e$ , (c) bulk velocity  $\mathbf{V}_e$ , (d) temperatures parallel ( $T_{e\parallel}$ ) and perpendicular ( $T_{e\perp}$ ) to  $\mathbf{B}$ , (e) heat flux  $\mathbf{q}_e$  in field-aligned components. (f) and (g) show 2D eVDFs  $f_e(v_{\parallel}, v_{\perp 1})$  (averaged over 1 second) taken from 13:19:35 and 13:20:33, respectively, where  $v_{\parallel} = \mathbf{v} \cdot \hat{\mathbf{b}}$  and  $v_{\perp 1} = \mathbf{v} \cdot (\hat{\mathbf{b}} \times (\hat{\mathbf{e}} \times \hat{\mathbf{b}}))$ , and  $\hat{\mathbf{b}} = \mathbf{B}/B$  and  $\hat{\mathbf{e}} = \mathbf{E}/E$  are the magnetic and electric field directions, respectively.

the electron heat flux in the MSH and its evolution from the BS to the MP. We also explore the effect of local heat flux regulation by investigating the relationship with whistler waves.

*Data and methods* - We use MMS data from the 2023 *unbiased magnetosheath campaign* [29], where 3 minutes of burst-mode data were sampled every 9 minutes providing 14 full inbound MSH crossings with a total of 13.9 hours of data. The fluxgate magnetometer (FGM) [40] provides the magnetic field vector  $\mathbf{B}$  and the Fast Plasma Investigation (FPI) [41] instruments give the full 3D eVDF every 30 ms. We use the highest-resolution burst-mode data to avoid effects of lossy compression of fast-mode data [42]. We pre-process the electron heat flux to remove non-physical noise originating from low-counting statistics. The noise removal algorithm, described in the Supplementary material, involves removing extreme values, correcting for the spacecraft spin tone, and smoothing the signal with a 1-second window.

*Results* - Figure 1 shows one of the 3-minute intervals from the MSH. Panels (a)-(d) show  $\mathbf{B}$ ,  $n_e$ ,  $\mathbf{V}_e$ , and parallel and perpendicular temperatures ( $T_{e\parallel}$ ,  $T_{e\perp}$  with respect to  $\mathbf{B}$ ), respectively. In the first half of the interval,  $B$  and  $n_e$  display an anti-correlation typical of

mirror-mode waves common in the quasi-perpendicular MSH configuration [43], where the mirror modes modulate  $T_{e\perp}$  [44]. Figure 1e shows the electron heat flux  $\mathbf{q}_e$  in field-aligned coordinates. The parallel component  $q_{e\parallel}$  dominates, consistent with approximately gyrotropic observed eVDFs. We note that  $\mathbf{q}_e$  changes direction in the vicinity of a sharp  $\mathbf{B}$  variation at 13:20:50. Figure 1f-g show the 2D eVDFs  $f_e(v_{\parallel}, v_{\perp 1})$  at two times: at 13:19:35, there is a parallel heat flux, and at 13:20:33, the heat flux is anti-parallel. The associated asymmetry is visible in  $f_e$ , especially in panel (g) where  $f_e$  is skewed towards negative  $v_{\parallel}$  at high energies. Thus, the heat flux can vary locally in the MSH, and its behavior is not directly predictable from other moments ( $n_e$ ,  $\mathbf{V}_e$ ,  $T_{e\parallel}$ , and  $T_{e\perp}$ ).

We now investigate whether local variations in the heat flux such as the one shown in Figure 1e accumulate to a significant change across the MSH. We quantify the large-scale heat flux with  $\langle q_e \rangle_{3\text{min}}$ , the mean magnitude of  $\mathbf{q}_e$  in each 3-minute burst interval. Figure 2a shows the locations of MMS in the geocentric solar ecliptic (GSE)  $XY$  plane with color and arrows indicating  $\langle q_e \rangle_{3\text{min}}$  and the mean vectors  $\langle \mathbf{q}_e \rangle_{3\text{min}}$ , respectively. The solid and dotted curves show models of the BS and MP, respectively, based on average SW conditions (retrieved from the OMNI database [45]) during the considered intervals, and the variation of their locations is indicated in gray (see details in Ref. [46]). The  $\mathbf{q}_e$  direction is tied to the magnetic field lines which are approximately aligned with the BS surface since the MSH is observed in a quasi-perpendicular configuration [30]. In each orbit,  $\langle q_e \rangle_{3\text{min}}$  does not change within the MSH with a few exceptions (e.g.,  $\langle q_e \rangle_{3\text{min}}$  increasing with BS distance in orbit #1 and the rotation in orbit #7). The SW conditions, such as the interplanetary magnetic field direction  $\hat{\mathbf{b}}_{\text{SW}}$ , are mostly stable during the individual orbits while in orbits where  $\hat{\mathbf{b}}_{\text{SW}}$  rotates, this is accompanied with rotation in  $\mathbf{q}_e$  (not shown). For two orbits #7 and #14 the MSH is highly compressed, with MSH measurements well within the average MP. This is due to a high-speed stream (orbit #7) and a coronal mass ejection (orbit #14). In both cases,  $\langle q_e \rangle_{3\text{min}}$  is 3-10 times higher than in the other orbits.

Figure 2b shows that  $\langle q_e \rangle_{3\text{min}}$  increases with the local MSH magnetic field strength  $B_{\text{MSH}}$ . The same dependence is seen with respect to  $B_{\text{SW}}$  (color scale) and with the SW dynamic pressure (see Supplementary material). The fit (black curve) based on the orbit-averages reveals that  $q_e$  is approximately proportional to  $B_{\text{MSH}}$ . Interestingly, this scaling with  $B$  is similar to previous observations in the SW at 1–5 AU (red circles, S94 [4]).

In Figure 2c, we study the  $\mathbf{q}_e$  evolution across the MSH using  $\langle q_e \rangle_{3\text{min}}$  normalized to the mean value in each orbit. We estimate the location relative to the MP and the BS with the fractional distance  $d_{\text{MP-BS}}$ , defined so that  $d_{\text{MP-BS}} = 0$  at the MP and  $d_{\text{MP-BS}} = 1$  at the BS [46, 47]. We show the individual orbits in red and the

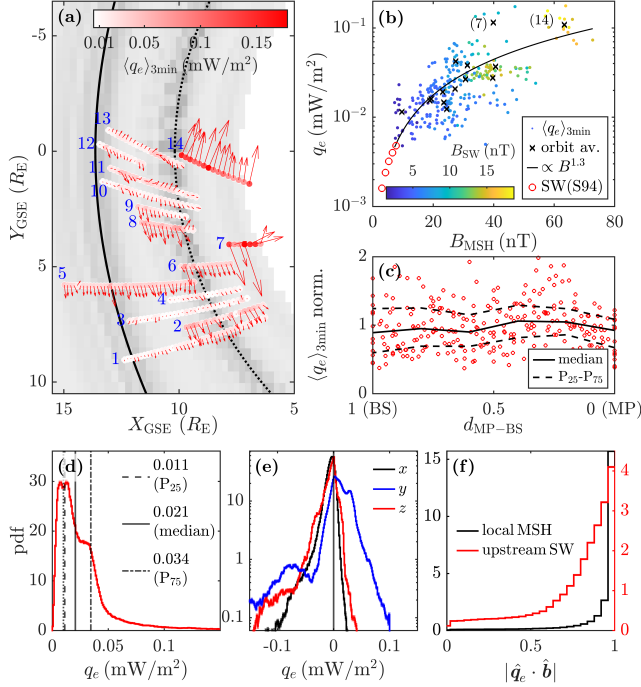


Figure 2. Electron heat flux across the MSH. (a) MMS location in each 3-minute burst interval in the GSE  $XY$  plane ( $Z_{\text{GSE}} \sim (-7, -5) R_E$ ). Color indicates  $\langle q_e \rangle_{3\text{min}}$ . Arrows show the projected  $\langle q_e \rangle_{3\text{min}}$ . Orbits are labeled chronologically 1-14 with blue numbers. (b)  $\langle q_e \rangle_{3\text{min}}$  versus  $B_{\text{MSH}}$ ; the color scale shows  $B_{\text{SW}}$ . Black curve shows the fit  $q_e \approx 3 \times 10^{-4} B^{1.3}$  based on the orbit-average values (black crosses). Red circles show approximate values of  $B$  and  $q_e$  from the SW, obtained by reading off the axes in Fig. 13 in Scime+ 1994 (S94) [4]. (c) Evolution of  $\langle q_e \rangle_{3\text{min}}$  (normalized to the mean in each orbit) with the fractional distance  $d_{\text{MP-BS}}$ . Solid curve shows the median in bins of width 0.2, and dashed curves show the 25<sup>th</sup> and 75<sup>th</sup> percentiles in the bins. Individual orbits are shown in red. (d) Overall  $q_e$  in the MSH; median value in solid, 25<sup>th</sup> and 75<sup>th</sup> percentiles in dashed and dash-dotted. Dotted line indicates the estimated uncertainty  $0.01 \text{ mW/m}^2$  (see Supplementary material). (e) GSE components of  $\mathbf{q}_e$ . (f) alignment of  $\hat{\mathbf{q}}_e = \mathbf{q}_e/q_e$  with the local magnetic field direction  $\hat{\mathbf{b}}_{\text{MSH}} = \mathbf{B}_{\text{MSH}}/B_{\text{MSH}}$  (black) and the upstream solar wind magnetic field direction  $\hat{\mathbf{b}}_{\text{SW}} = \mathbf{B}_{\text{SW}}/B_{\text{SW}}$  (red).

black curves show the median (solid), 25<sup>th</sup> and 75<sup>th</sup> percentiles (dashed) in bins of width  $d_{\text{MP-BS}} = 0.2$ . While there is a large variation across different orbits, there is no clear evolution of the normalized  $\langle q_e \rangle_{3\text{min}}$  with  $d_{\text{MP-BS}}$ , indicating that the electron heat flux is not significantly created or destroyed in the MSH.

Figure 2d-f shows histograms of  $\mathbf{q}_e$  without time averaging, i.e., obtained from the entire dataset, corresponding to 1,671,203 eVDFs. The median  $q_e$  is  $0.021 \text{ mW/m}^2$  and 50% of the data is within  $0.012$  and  $0.035 \text{ mW/m}^2$  (see Figure 2d). This is slightly higher than reported values of  $0.005$ – $0.01 \text{ mW/m}^2$  in the SW at 1 AU [4, 48, 49]. The  $x$  component is negative ( $q_{ex} < 0$ ; black in Fig-

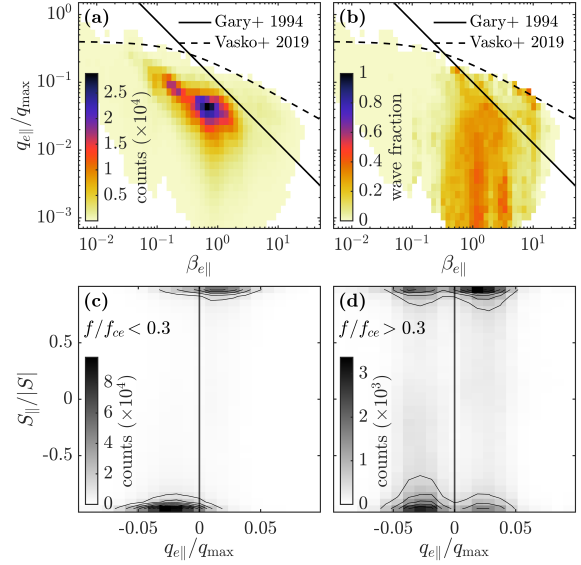


Figure 3. Whistler heat flux instabilities. (a) 2D histogram of  $|q_{e\parallel}|/q_{\text{max}}$  and  $\beta_{e\parallel}$  with each count corresponding to one 30 ms electron measurement. (b) Whistler wave occurrence in the  $\beta_{e\parallel} - |q_{e\parallel}|/q_{\text{max}}$  parameter space. We show two whistler instability thresholds: the parallel heat flux instability (solid: Gary+ 1994 [9]:  $|q_{e\parallel}|/q_{\text{max}} = 0.10\beta_{e\parallel}^{-0.90}$  for a growth rate  $\gamma = 10^{-3}\Omega_p$ , where  $\Omega_p$  is the angular proton cyclotron frequency) and the oblique heat flux fan instability (dashed: Vasko+ 2019 [36]:  $|q_{e\parallel}|/q_{\text{max}} = 0.20 [\beta_{e\parallel} + 0.25]^{-0.50}$ ). (c) Poynting flux of low-frequency whistler waves ( $f/f_{ce} < 0.3$ ) versus  $q_{e\parallel}/q_{\text{max}}$ . (d) Same as (c) but for high-frequency ( $f/f_{ce} > 0.3$ ) whistler waves.

ure 2e) similar to the anti-sunward strahl in the SW. Its southward direction ( $q_{ez} < 0$ ; red curve) indicates that the heat flux is directed around the magnetosphere since MMS is located at  $Z_{\text{GSE}} < 0$  during the entire dataset (not shown). As expected for approximately gyrotropic distributions,  $\mathbf{q}_e$  is aligned with the local magnetic field ( $|\hat{\mathbf{q}}_e \cdot \hat{\mathbf{b}}_{\text{MSH}}| \approx 1$ , black in Figure 2f). Moreover, the heat flux follows the magnetic field draping around the magnetosphere, since  $|\hat{\mathbf{q}}_e \cdot \hat{\mathbf{b}}_{\text{SW}}|$  is biased towards 1 (Figure 2f).

To understand how the heat flux is regulated in the magnetosheath, we compare the heat flux distribution to instability thresholds for the whistler heat flux instability, which is the most likely instability since  $\beta_{e\parallel} \gtrsim 0.1$  in our dataset [9]. Figure 3a shows the  $\beta_{e\parallel} - |q_{e\parallel}|/q_{\text{max}}$  parameter space, where  $q_{\text{max}} = \frac{3}{2} m_e n_e v_{\text{th}}^3$  is the free-streaming heat flux [3] and  $v_{\text{th}} = \sqrt{T_e/m_e}$  is the thermal speed. We show the instability threshold for parallel propagating waves (solid) [9] and oblique waves (dashed) [36], The data is bounded by these thresholds, suggesting that the whistler instability regulates the heat flux in the MSH.

To further explore the role of whistler instabilities, we compare the heat flux to whistler wave packets analyzed previously in Ref. [30]. The wave packets are mainly found parallel-propagating with respect to  $\mathbf{B}$

and appear in two frequency bands; the majority with  $f/f_{ce} \in (0.1, 0.3)$  and a smaller population with  $f/f_{ce} \in (0.3, 0.6)$ , where  $f_{ce} = eB/(2\pi m_e)$  is the electron cyclotron frequency [30]. In Figure 3b we show the fraction of data points in the MSH during which whistler wave packets are observed. Whistler activity is mainly observed for  $\beta_{e\parallel} > 0.1$  as noted in Ref. [30]. Apart from an increased wave activity at the oblique instability threshold (dashed) for  $\beta_{e\parallel} \approx 10$ , whistler activity does not correlate with a high heat flux close to the instability thresholds. However, the whistler wave distribution follows the parallel whistler instability threshold (solid), suggesting that there is a connection between heat flux and whistler waves.

In general, due to the asymmetry of the eVDF, whistler waves produced by the heat flux instability propagate along the magnetic field in the same direction as the heat flux [50], while the temperature anisotropy instability generates both parallel and anti-parallel waves. Therefore, we investigate the wave propagation direction using the Poynting flux  $\mathcal{S}$ , which is parallel to the group velocity. Figure 3c shows  $S_{\parallel}/|\mathcal{S}|$ , the normalized parallel Poynting flux with respect to  $\mathbf{B}$ , versus  $q_{e\parallel}/q_{\max}$ , for low-frequency ( $f/f_{ce} < 0.3$ ) whistler wave packets, i.e., where the majority of the observed waves are found. The clustering in the top right and bottom left corners indicates that the wave packets are predominantly aligned with the heat flux, consistent with the whistler heat flux instability. On the other hand, the propagation of high-frequency waves ( $f/f_{ce} > 0.3$ ; Figure 3d) has less alignment with  $q_{e\parallel}$ .

*Discussion* - In this Letter, we statistically analyze the electron heat flux across the MSH, from the BS to the MP. We find that the heat flux in the MSH shares traits of the heat flux in the upstream SW, as it is mainly field-aligned, has an anti-sunward component. Some properties are altered; most notably, the direction follows the field line draping around the magnetosphere and the magnitude is higher than typical values in the solar wind, especially when the magnetic field is strong. Due to the order-of-magnitude variations between different orbits, the upstream conditions likely impact the heat flux downstream of the bow shock. Importantly, both cases of highly compressed MSH show significantly higher values compared to other orbits.

We find that  $q_e$  increases proportionally to the local magnetic field strength  $B_{\text{MSH}}$  and the upstream  $B_{\text{SW}}$ . A correlation between  $q_e$  and  $B_{\text{SW}}$  has been observed in the SW at 1–5 AU [4]; however, this was also a radial effect as both  $q_e$  and  $B$  decrease with distance from the sun. In this work, the reason for the proportionality is not clear. Possibly the correlation exists in the SW even at 1 AU. Moreover, considering the high  $q_e$  in the MSH compared to the SW, it seems that  $q_e$  increases at the BS. With the present dataset, we cannot determine the relative impacts of upstream conditions and shock accel-

eration processes. This requires larger datasets as well as continuous  $q_e$  measurements from the SW to the MSH.

The magnitude of the electron heat flux remains relatively steady within the MSH during individual orbits. Although it can vary locally, the cumulative effect of potential sources and sinks does not globally affect the heat flux magnitude. One potential source for heat flux is magnetic reconnection at the MP [8]. However, we do not observe an increase of heat flux close to this boundary ( $d_{\text{MP-BS}} \approx 0$ ). This suggests that the heat flux created at the MP remains in the vicinity of the MP.

The heat flux is limited by the parallel [9] and oblique [36] whistler instability thresholds. However, we find that there is no increase in whistler wave activity when the heat flux is close to the instability thresholds. As the same instabilities bound the heat flux in the SW [6, 9, 51], the fact that the heat flux is constrained by these instability thresholds can be a remainder of SW dynamics, where the heat flux has already been actively regulated by the whistler instability.

On the other hand, a possible whistler-heat flux instability is supported by the alignment between low-frequency ( $f/f_{ce} < 0.3$ ) whistlers and the heat flux direction. Also, the wave occurrence is constrained by the parallel whistler instability, similarly to what has been observed in the SW [51]. Thus, this instability cannot be out-ruled. One possibility is that the asymmetric features typical of the heat flux instability exist in the whistler-resonant parts of the eVDF (satisfying the first-order cyclotron resonance condition, typically a few times the thermal energy [30]). The heat flux calculated from the entire distribution may not necessarily predict an instability. Considering the agreement with instability thresholds and the directional alignment, we suggest that the heat flux whistler instabilities play a role in the MSH.

For a reliable estimation of the electron heat flux, the analysis presented here required removing noise, non-physical data spikes, and correcting for a spin signal (see Supplementary material). Previously, the heat flux has been obtained from the eVDF with another method [8], by restricting the energy range and estimating the errors from Poisson statistics. However, this is more suitable for case studies due to the heavy processing of the full eVDF at each time step. Our approach provides an alternative better suited for statistical studies when a large amount of data needs to be processed.

*Conclusions* - The electron heat flux is important for understanding energy conversion in space, astrophysical and laboratory plasma. Using 13.9 hours of burst-mode data from the Magnetospheric Multiscale (MMS) mission, we statistically study the electron heat flux downstream of the Earth's bow shock, how it evolves inside the magnetosheath, and its potential regulation by whistler instabilities. We find that the magnetosheath electron heat flux is slightly higher than that in the solar wind at 1 AU and that it drapes around the magnetosphere

following the magnetic field lines. Its magnitude varies with upstream solar wind conditions and increases with magnetic field strength. However, local processes in the magnetosheath do not substantially change the heat flux during propagation from the bow shock to the magnetopause. The heat flux is constrained by the parallel and oblique whistler instability thresholds, and the alignment of low-frequency whistler wave propagation with the heat flux direction further supports a connection between electron heat flux and whistler waves.

These findings have broader implications for understanding heat flux regulation in high-beta plasmas such as those found in supernova remnants, the outer solar corona, and the interstellar medium [52], which are not accessible for *in situ* measurements. Our results thus provide a valuable contribution to the understanding the global energy budget in the MSH and can also serve as a reference for modelling the electron heat flux in high-beta, compressible plasmas.

*Acknowledgments* - MMS data are available at the MMS Science Data Center [53]. Data analysis was performed using the `irfu-matlab` package [54]. We thank the MMS team and instrument PIs for data access and support. We thank Heli Hietala and Istvan Pusztai for valuable input. We acknowledge support from the Swedish Research Council Grant 20160550 and the Swedish National Space Agency Grants 158/16 and 192/20. This research was supported by the International Space Science Institute (ISSI) in Bern, through the ISSI International Team project #23-588 ('Unveiling Energy Conversion and Dissipation in Non-Equilibrium Space Plasmas'). The work was supported by the Knut and Alice Wallenberg foundation (Dnr. 2022.0087). The work of GC is supported by the Integration Fellowship of Le Studium Loire Valley Institute for Advanced Studies.

- 
- [1] D. Verscharen, R. T. Wicks, O. Alexandrova, R. Bruno, D. Burgess, C. H. K. Chen, R. D'Amicis, J. De Keyser, T. D. De Wit, L. Franci, J. He, P. Henri, S. Kasahara, Y. Khotyaintsev, K. G. Klein, B. Lavraud, B. A. Maruca, M. Maksimovic, F. Plaschke, S. Poedts, C. S. Reynolds, O. Roberts, F. Sahraoui, S. Saito, C. S. Salem, J. Saur, S. Servidio, J. E. Stawarz, . tverk, and D. Told, *Experimental Astronomy* **54**, 473 (2022).
- [2] L. Spitzer and R. Hrm, *Physical Review* **89**, 977 (1953).
- [3] S. D. Bale, M. Pulupa, C. Salem, C. H. K. Chen, and E. Quataert, *The Astrophysical Journal* **769**, L22 (2013).
- [4] E. E. Scime, S. J. Bame, W. C. Feldman, S. P. Gary, J. L. Phillips, and A. Balogh, *Journal of Geophysical Research: Space Physics* **99**, 23401 (1994).
- [5] G. T. Roberg-Clark, J. F. Drake, M. Swisdak, and C. S. Reynolds, *The Astrophysical Journal* **867**, 154 (2018).
- [6] J. S. Halekas, P. L. Whittlesey, D. E. Larson, D. McGinnis, S. D. Bale, M. Berthomier, A. W. Case, B. D. G. Chandran, J. C. Kasper, K. G. Klein, K. E. Korreck, R. Livi, R. J. MacDowall, M. Maksimovic, D. M. Malaspina, L. Matteini, M. P. Pulupa, and M. L. Stevens, *Astronomy & Astrophysics* **650**, A15 (2021).
- [7] J. T. Coburn, D. Verscharen, C. J. Owen, M. Maksimovic, T. S. Horbury, C. H. K. Chen, F. Guo, X. Fu, J. Liu, J. B. Abraham, G. Nicolaou, M. E. Innocenti, A. Micera, and V. K. Jagarlamudi, *The Astrophysical Journal* **964**, 100 (2024).
- [8] D. J. Gershman, L. Chen, A. Le, J. Shuster, J. C. Dorelli, J. Ng, B. Giles, A. F. Vias, R. Torbert, and J. L. Burch, *Geophysical Research Letters* **51**, e2024GL109783 (2024).
- [9] S. P. Gary, E. E. Scime, J. L. Phillips, and W. C. Feldman, *Journal of Geophysical Research* **99**, 23391 (1994).
- [10] S. P. Gary, R. M. Skoug, and W. Daughton, *Physics of Plasmas* **6**, 2607 (1999).
- [11] F. Finelli, S. S. Cerri, F. Califano, F. Pucci, D. Laveder, G. Lapenta, and T. Passot, *Astronomy & Astrophysics* **653**, A156 (2021).
- [12] P. L. Sulem and T. Passot, *Journal of Plasma Physics* **81**, 325810103 (2015).
- [13] Z. Huang, C. Dong, and L. Wang, *Proceedings of the National Academy of Sciences* **122**, e2419073122 (2025).
- [14] E. R. Ingelsten, M. C. McGrae-Menge, E. P. Alves, and I. Pusztai, *Journal of Plasma Physics* **91**, E64 (2025).
- [15] D. B. Graham, Y. V. Khotyaintsev, M. Andr, A. Vaivads, A. Chasapis, W. H. Matthaeus, A. Retin, F. Valentini, and D. J. Gershman, *Journal of Geophysical Research: Space Physics* **126**, 10.1029/2021JA029260 (2021).
- [16] M. Pohl and J. A. Esposito, *The Astrophysical Journal* **507**, 327 (1998).
- [17] S. W. Kahler, *Space Science Reviews* **129**, 359 (2007).
- [18] L. Yang, L. Wang, G. Li, R. F. Wimmer-Schweingruber, J. He, C. Tu, H. Tian, and S. D. Bale, *The Astrophysical Journal* **853**, 89 (2018).
- [19] J. L. Phillips, S. J. Bame, M. F. Thomsen, B. E. Goldstein, and E. J. Smith, *Journal of Geophysical Research: Space Physics* **98**, 21189 (1993).
- [20] G. Andreone, J. S. Halekas, D. L. Mitchell, C. Mazelle, and J. Gruesbeck, *Journal of Geophysical Research: Space Physics* **127**, e2021JA029404 (2022).
- [21] T. Amano, M. Masuda, M. Oka, N. Kitamura, O. Le Contel, and D. J. Gershman, *Physics of Plasmas* **31**, 042903 (2024).
- [22] A. Lalti, Y. V. Khotyaintsev, and D. B. Graham, *Geophysical Research Letters* **51**, e2024GL112547 (2024).
- [23] A. Retin, D. Sundkvist, A. Vaivads, F. Mozer, M. Andr, and C. J. Owen, *Nature Physics* **3**, 235 (2007).
- [24] E. Yordanova, Z. Vrs, A. Varsani, D. B. Graham, C. Norgren, Y. V. Khotyaintsev, A. Vaivads, E. Eriksson, R. Nakamura, P.-A. Lindqvist, G. Marklund, R. E. Ergun, W. Magnes, W. Baumjohann, D. Fischer, F. Plaschke, Y. Narita, C. T. Russell, R. J. Strangeway, O. Le Contel, C. Pollock, R. B. Torbert, B. J. Giles, J. L. Burch, L. A. Avanov, J. C. Dorelli, D. J. Gershman, W. R. Paterson, B. Lavraud, and Y. Saito, *Geophysical Research Letters* **43**, 5969 (2016).
- [25] Z. Vrs, E. Yordanova, A. Varsani, K. J. Genestreti, Y. V. Khotyaintsev, W. Li, D. B. Graham, C. Norgren, R. Nakamura, Y. Narita, F. Plaschke, W. Magnes, W. Baumjohann, D. Fischer, A. Vaivads, E. Eriksson, P. Lindqvist, G. Marklund, R. E. Ergun, M. Leitner, M. P. Leubner, R. J. Strangeway, O. LeContel, C. Pollock, B. J. Giles, R. B. Torbert, J. L. Burch, L. A.

- Avanov, J. C. Dorelli, D. J. Gershman, W. R. Paterson, B. Lavraud, and Y. Saito, *Journal of Geophysical Research: Space Physics* **122**, 10.1002/2017JA024535 (2017).
- [26] T. D. Phan, J. P. Eastwood, M. A. Shay, J. F. Drake, B. U. . Sonnerup, M. Fujimoto, P. A. Cassak, M. Ieroset, J. L. Burch, R. B. Torbert, A. C. Rager, J. C. Dorelli, D. J. Gershman, C. Pollock, P. S. Pyakurel, C. C. Haggerty, Y. Khotyaintsev, B. Lavraud, Y. Saito, M. Oka, R. E. Ergun, A. Retino, O. Le Contel, M. R. Argall, B. L. Giles, T. E. Moore, F. D. Wilder, R. J. Strangeway, C. T. Russell, P. A. Lindqvist, and W. Magnes, *Nature* **557**, 202 (2018).
- [27] J. E. Stawarz, J. P. Eastwood, T. D. Phan, I. L. Gingell, M. A. Shay, J. L. Burch, R. E. Ergun, B. L. Giles, D. J. Gershman, O. L. Contel, P.-A. Lindqvist, C. T. Russell, R. J. Strangeway, R. B. Torbert, M. R. Argall, D. Fischer, W. Magnes, and L. Franci, *The Astrophysical Journal Letters* **877**, L37 (2019).
- [28] J. E. Stawarz, J. P. Eastwood, T. D. Phan, I. L. Gingell, P. S. Pyakurel, M. A. Shay, S. L. Robertson, C. T. Russell, and O. Le Contel, *Physics of Plasmas* **29**, 012302 (2022).
- [29] I. Svenningsson, E. Yordanova, G. Cozzani, Y. V. Khotyaintsev, and M. Andr, *Geophysical Research Letters* **49**, 10.1029/2022GL099065 (2022).
- [30] I. Svenningsson, E. Yordanova, Y. V. Khotyaintsev, M. Andr, G. Cozzani, and K. Steinvall, *Journal of Geophysical Research: Space Physics* **129**, e2024JA032661 (2024).
- [31] C. H. K. Chen, K. G. Klein, and G. G. Howes, *Nature Communications* **10**, 740 (2019).
- [32] A. S. Afshari, G. G. Howes, J. R. Shuster, K. G. Klein, D. McGinnis, M. M. Martinovi, S. A. Boardsen, C. R. Brown, R. Huang, D. P. Hartley, and C. A. Kletzing, *Nature Communications* **15**, 7870 (2024).
- [33] H. Breuillard, O. LeContel, T. Chust, M. Berthomier, A. Retino, D. L. Turner, R. Nakamura, W. Baumjohann, G. Cozzani, F. Catapano, A. Alexandrova, L. Mirioni, D. B. Graham, M. R. Argall, D. Fischer, F. D. Wilder, D. J. Gershman, A. Varsani, P. Lindqvist, Y. V. Khotyaintsev, G. Marklund, R. E. Ergun, K. A. Goodrich, N. Ahmadi, J. L. Burch, R. B. Torbert, G. Needell, M. Chutter, D. Rau, I. Dors, C. T. Russell, W. Magnes, R. J. Strangeway, K. R. Bromund, H. Wei, F. Plaschke, B. J. Anderson, G. Le, T. E. Moore, B. L. Giles, W. R. Paterson, C. J. Pollock, J. C. Dorelli, L. A. Avanov, Y. Saito, B. Lavraud, S. A. Fuselier, B. H. Mauk, I. J. Cohen, and J. F. Fennell, *Journal of Geophysical Research: Space Physics* **123**, 93 (2018).
- [34] W. Gonzalez and E. Parker, eds., *Magnetic Reconnection: Concepts and Applications*, Astrophysics and Space Science Library, Vol. 427 (Springer International Publishing, Cham, 2016).
- [35] J. L. Burch, T. E. Moore, R. B. Torbert, and B. L. Giles, *Space Science Reviews* **199**, 5 (2016).
- [36] I. Y. Vasko, V. Krasnoselskikh, Y. Tong, S. D. Bale, J. W. Bonnell, and F. S. Mozer, *The Astrophysical Journal Letters* **871**, L29 (2019).
- [37] A. Micera, A. N. Zhukov, R. A. Lopez, M. E. Innocenti, M. Lazar, E. Boella, and G. Lapenta, *The Astrophysical Journal Letters* **903**, L23 (2020).
- [38] S. P. Gary and J. Wang, *Journal of Geophysical Research: Space Physics* **101**, 10749 (1996).
- [39] N. Kitamura, Y. Omura, S. Nakamura, T. Amano, S. A. Boardsen, N. Ahmadi, O. Le Contel, P. Lindqvist, R. E. Ergun, Y. Saito, S. Yokota, D. J. Gershman, W. R. Paterson, C. J. Pollock, B. L. Giles, C. T. Russell, R. J. Strangeway, and J. L. Burch, *Journal of Geophysical Research: Space Physics* **125**, 10.1029/2019JA027488 (2020).
- [40] C. T. Russell, B. J. Anderson, W. Baumjohann, K. R. Bromund, D. Dearborn, D. Fischer, G. Le, H. K. Leinweber, D. Leneman, W. Magnes, J. D. Means, M. B. Moldwin, R. Nakamura, D. Pierce, F. Plaschke, K. M. Rowe, J. A. Slavin, R. J. Strangeway, R. Torbert, C. Hagen, I. Jernej, A. Valavanoglou, and I. Richter, *Space Science Reviews* **199**, 189 (2016).
- [41] C. Pollock, T. Moore, A. Jacques, J. Burch, U. Gliese, Y. Saito, T. Omoto, L. Avanov, A. Barrie, V. Coffey, J. Dorelli, D. Gershman, B. Giles, T. Rosnack, C. Salo, S. Yokota, M. Adrian, C. Aoustin, C. Auletta, S. Aung, V. Bigio, N. Cao, M. Chandler, D. Chornay, K. Christian, G. Clark, G. Collinson, T. Corris, A. DeLosSantos, R. Devlin, T. Diaz, T. Dickerson, C. Dickson, A. Diekmann, F. Diggs, C. Duncan, A. Figueroa-Vinas, C. Firman, M. Freeman, N. Galassi, K. Garcia, G. Goodhart, D. Guererro, J. Hageman, J. Hanley, E. Hemminger, M. Holland, M. Hutchins, T. James, W. Jones, S. Kreisler, J. Kujawski, V. Lavu, J. Lobell, E. LeCompte, A. Lukemire, E. MacDonald, A. Mariano, T. Mukai, K. Narayanan, Q. Nguyen, M. Onizuka, W. Paterson, S. Persyn, B. Piepgrass, F. Cheney, A. Rager, T. Raghuram, A. Ramil, L. Reichenthal, H. Rodriguez, J. Rouzaud, A. Rucker, Y. Saito, M. Samara, J.-A. Sauvaud, D. Schuster, M. Shappirio, K. Shelton, D. Sher, D. Smith, K. Smith, S. Smith, D. Steinfeld, R. Szymkiewicz, K. Tanimoto, J. Taylor, C. Tucker, K. Tull, A. Uhl, J. Vloet, P. Walpole, S. Weidner, D. White, G. Winkert, P.-S. Yeh, and M. Zeuch, *Space Science Reviews* **199**, 331 (2016).
- [42] A. C. Barrie, D. L. Smith, S. R. Elkington, Z. Sternovsky, D. Silva, B. L. Giles, and C. Schiff, *Earth and Space Science* **6**, 116 (2019).
- [43] A. P. Dimmock, A. Osmane, T. I. Pulkkinen, and K. Nykyri, *Journal of Geophysical Research: Space Physics* **120**, 5489 (2015).
- [44] S. T. Yao, Q. Q. Shi, J. Liu, Z. H. Yao, R. L. Guo, N. Ahmadi, A. W. Degeling, Q. G. Zong, X. G. Wang, A. M. Tian, C. T. Russell, H. S. Fu, Z. Y. Pu, S. Y. Fu, H. Zhang, W. J. Sun, L. Li, C. J. Xiao, Y. Y. Feng, and B. L. Giles, *Journal of Geophysical Research: Space Physics* **123**, 5561 (2018).
- [45] N. E. Papitashvili and J. H. King, *NASA Space Physics Data Facility* <https://doi.org/10.48322/1shr-ht18> (2020).
- [46] I. Svenningsson, E. Yordanova, Y. V. Khotyaintsev, M. Andr, and G. Cozzani, *Journal of Geophysical Research: Space Physics* **130**, e2024JA033272 (2025).
- [47] A. P. Dimmock and K. Nykyri, *Journal of Geophysical Research: Space Physics* **118**, 4963 (2013).
- [48] C. A. Cattell, B. Short, A. W. Breneman, and P. Grul, *The Astrophysical Journal* **897**, 126 (2020).
- [49] C. S. Salem, M. Pulupa, S. D. Bale, and D. Verscharen, *Astronomy & Astrophysics* **675**, A162 (2023).
- [50] D. Verscharen, B. D. G. Chandran, E. Boella, J. Halekas, M. E. Innocenti, V. K. Jagarlamudi, A. Micera, V. Pierard, . tverk, I. Y. Vasko, M. Velli, and P. L. Whittlesey, *Frontiers in Astronomy and Space Sciences* **9**, 951628

- (2022).
- [51] C. Cattell, A. Breneman, J. Dombeck, E. Hanson, M. Johnson, J. Halekas, S. D. Bale, T. Dudok De Wit, K. Goetz, K. Goodrich, D. Malaspina, M. Pulupa, T. Case, J. C. Kasper, D. Larson, M. Stevens, and P. Whittlesey, *The Astrophysical Journal Letters* **924**, L33 (2022).
- [52] A. Vaivads, A. Retin, and M. Andr, *Plasma Physics and Controlled Fusion* **51**, 124016 (2009).
- [53] See <https://lasp.colorado.edu/mms/sdc/public>.
- [54] See <https://github.com/irfu/irfu-matlab>.

**Supplemental materials to the manuscript**  
**Electron Heat Flux and Whistler Instability in the Earth's Magnetosheath**  
 by I. Svenningsson et al.

**HEAT FLUX NOISE REMOVAL METHOD**

The heat flux is a 3<sup>rd</sup> order moment of the electron velocity distribution function, and therefore more sensitive to counting statistics than lower-order moments such as the velocity. Therefore, the calibrated data product contains noise which must be considered before using the data. Figure S1 shows how we remove noise in a 3-minute interval from our dataset. Figure S1a and b show the magnetic field  $\mathbf{B}$  and heat flux  $\mathbf{q}_e$ , respectively, as obtained from the MMS L2 data products.

First, we remove noise spikes. In 1-second windows (containing 33 values), we calculate the median  $M$  and standard deviation  $\sigma$ . We then remove values that are more than  $1\sigma$  away from  $M$  and interpolate between the closest values that we keep. The result of this step is shown in Figure S1c.

Each MMS spacecraft spins around its own axis with a period of 20 seconds, which can create a spin-tone signature in the data products. This example in particular has a clear spin tone visible in Figure S1c. To remove this artifact, we apply a narrow band-pass filter around the

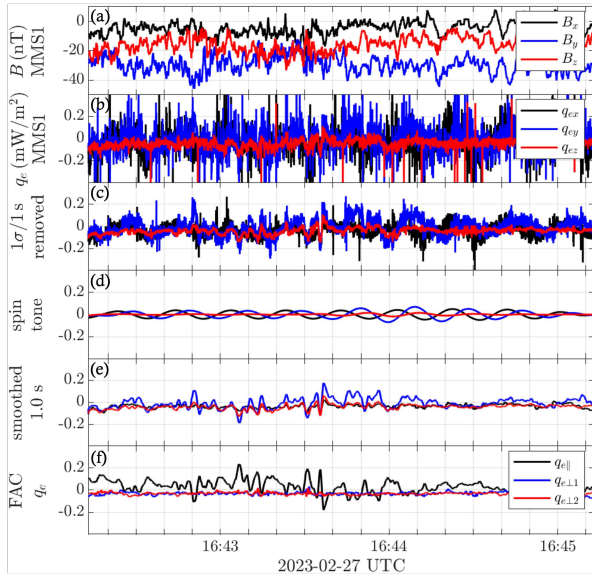


FIG. S1: One of the 3-minute intervals from our dataset. (a) Magnetic field vector  $\mathbf{B}$ . (b) Heat flux vector before applying the noise removal. (c) Heat flux with noise spikes removed; spin-tone signal (d) Spin tone found by band-pass filtering (e) between  $0.95f_{\text{spin}}$  and  $1.05f_{\text{spin}}$  where  $f_{\text{spin}} = 1/(20\text{ s})$ . (e) Heat flux with spin tone removed and smoothed with a 1-second window. (f) Heat flux vector in field-aligned coordinates with respect to  $\mathbf{B}$ .

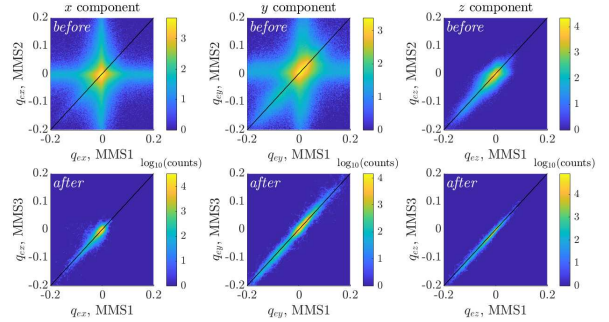


FIG. S2: Comparison of  $\mathbf{q}_e$  measured by MMS1&2 before (top row) and after (bottom row) applying the noise removal method. The columns show the GSE  $x$ ,  $y$ , and  $z$  components.

spin frequency and obtain the spin-tone estimation shown in Figure S1d. We subtract this signal and smooth the result with a 1-second window. Figure S1e shows the resulting signal which we use in the main text. Figure S1f shows the same signal in field-aligned coordinates with respect to  $\mathbf{B}$ .

We also cross-checked that the 3 MMS spacecraft with available electron measurements give overall consistent values. This is indeed the case, in contrast to before applying the above-described method. We show the difference in Figure S2.

**UNCERTAINTY LEVEL ESTIMATION**

We use two methods to estimate a uncertainty amplitude for  $q_{e\parallel}$  after applying the method described above. First, since the heat flux is expected to be field-aligned, we check the amplitude of the perpendicular components  $q_{e\perp 1}$  and  $q_{e\perp 2}$  (see Figure S3a-c). In addition, since the spin tone is not sinusoidal, removing only the 20-second component of the spin tone can leave behind higher-frequency content. We estimate an upper bound to the remaining spin signal error using the amplitude of the removed signal (see Figure S3d-f). Both methods give an estimated uncertainty level of  $\sim 0.01\text{ mW/m}^2$ .

**PARAMETER DEPENDENCIES**

We look for correlations between the electron heat flux and other SW and MSH parameters. The only clear correlation was with the magnetic field strength (see Figure 2b the main text) and the upstream dynamic pressure. In Figure S4, we show how the heat flux varies with

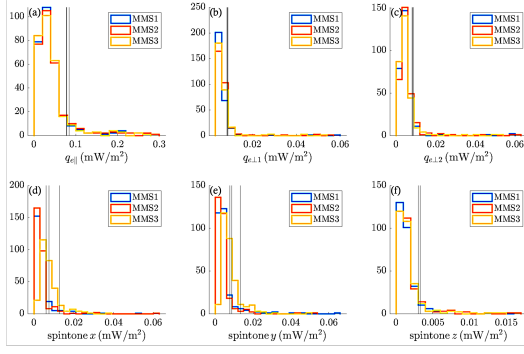


FIG. S3: Top row (a-c): histograms of  $q_e$  in the parallel and two perpendicular components to  $\mathbf{B}$  as given by MMS1-3. The vertical lines show the 90<sup>th</sup> percentiles. In the perpendicular components, this value is  $\sim 0.01$  mW/m<sup>2</sup>. Bottom row (d-f): histograms of the spin tone amplitude (see Figure S1d). In MMS1-2, this value is  $\sim 0.01$  mW/m<sup>2</sup>.

other parameters. The SW values and Alfvénic Mach number are taken from the OMNI [1] database based on L1 measurements. The shock normal angle is calculated based on upstream magnetic field direction and a model bow shock [see details in 2]. The MSH values are based on MMS measurements. The blue circles show the average during the orbit (full MSH crossing) and the red dots show 3-minute average values.

- [1] N. E. Papitashvili and J. H. King, NASA Space Physics Data Facility (2020).  
 [2] I. Svenningsson, E. Yordanova, Y. V. Khotyaintsev, M. André, and G. Cozzani, Journal of Geophysical Research: Space Physics **130**, e2024JA033272 (2025), ISSN 2169-9380, 2169-9402, URL <https://agupubs.onlinelibrary.wiley.com/doi/10.1029/2024JA033272>.

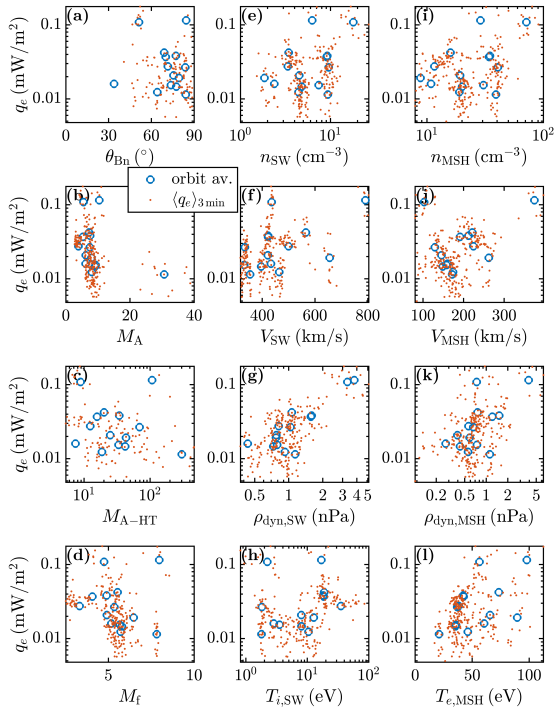


FIG. S4: Electron heat flux magnitude as a function of upstream and local parameters. (a) Shock normal angle  $\theta_{Bn}$ . (b) Upstream Alfvénic Mach number  $M_A$ . (c) Upstream Alfvénic Mach number in the de Hoffman-Teller frame  $M_{A-HT} = M_A / \cos \theta_{Bn}$ . (d) Upstream fast magnetosonic Mach number  $M_f$ . (e) SW ion density  $n_{SW}$ . (f) SW speed  $V_{SW}$ . (g) SW dynamic pressure  $\rho_{dyn,SW} = \frac{1}{2} \rho_{SW} V_{SW}^2$ , where  $\rho_{SW}$  is the mass density assuming 4 % helium abundance. (h) SW ion temperature  $T_{i,SW}$ . (i) MSH ion density  $n_{MSH}$ . (j) MSH speed  $V_{MSH}$ . (k) MSH dynamic pressure  $\rho_{dyn,MSH}$  (defined similar to  $\rho_{dyn,SW}$ ). (l) MSH electron temperature  $T_{e,SW}$ .